Supplementary Figures

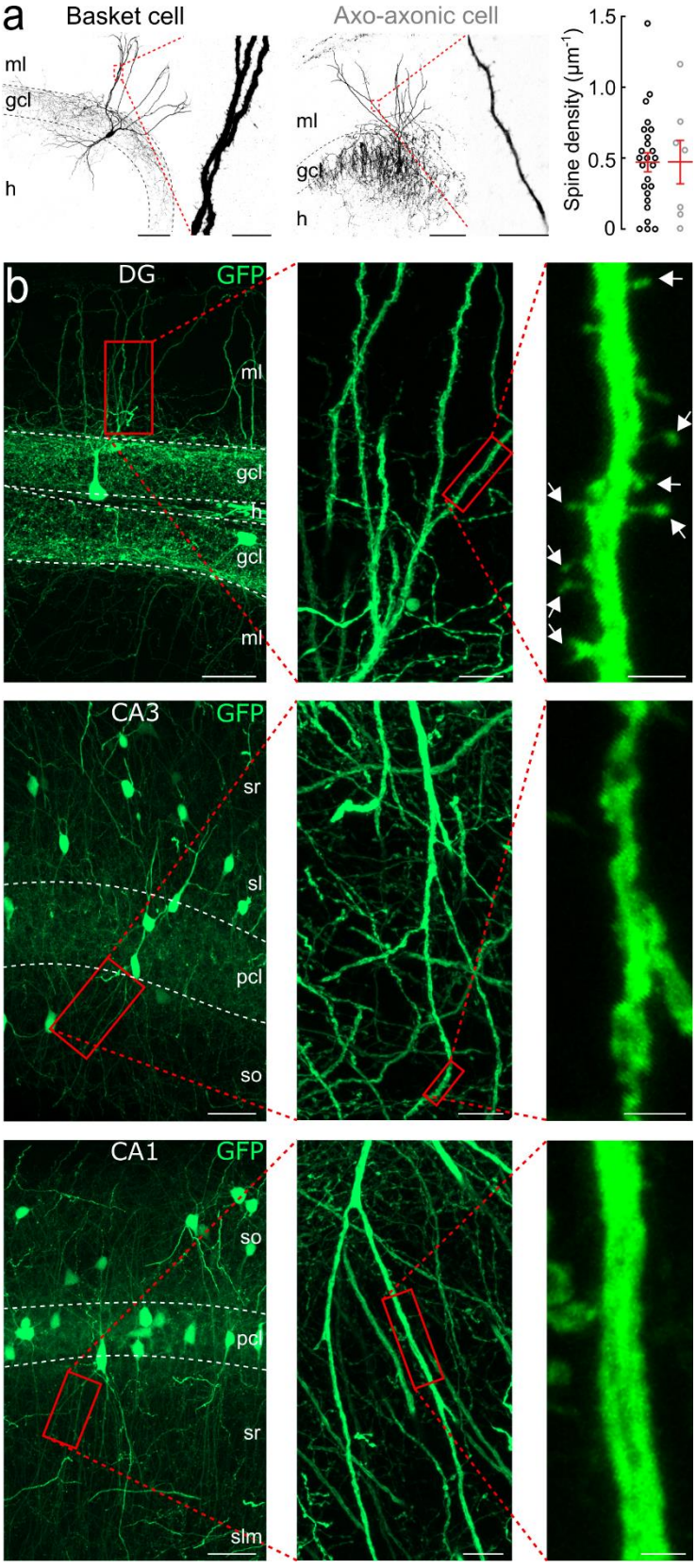

Supplementary Figure 1: Basket and axo-axonic cells express spines in the DG but rarely in CA1-3. **a** *Left,* confocal maximal intensity projection of a basket and axo-axonic cell filled with biocytin during recordings. Red square depicts dendritic areas shown at higher magnification on the right for each cell to highlight spines. *Right*, both cell types show similar mean spine densities at their apical dendrites (P=0.997, unpaired two-sided t-test; 25 basket and 7 axo-axonic cells)**. b** Confocal images of hippocampal (*top*) DG, (*middle*) CA3 and (*bottom*) CA1 PVIs expressing AAV-FLEX-GFP. Areas defined by red squares are shown at higher magnifications on the right. Selected dendritic segments (red squares) are further magnified on the right. PVI spines (white arrows) were unequivocally identified in the DG, but they appeared rarely in CA3 or CA1. Red lines represent mean ± SEM. Scale bars in (a) overview 100 µm, for dendrites 10 µm; (b) left 50 µm, middle 10 µm, right 2 µm. Circles in (a) represents the spine density for that dendritic segments of individual PVIs, which showed the highest spine density. Highest PVI spine densities in the dDG were always observed in the inner ml. Abbreviations: gcl, granule cell layer; h, hilus; ml, molecular layer; pcl, pyramidal cell layer; sl, stratum lucidum; slm, stratum lacunosmum moleculare; so, stratum oriens; sr, stratum radiatum;

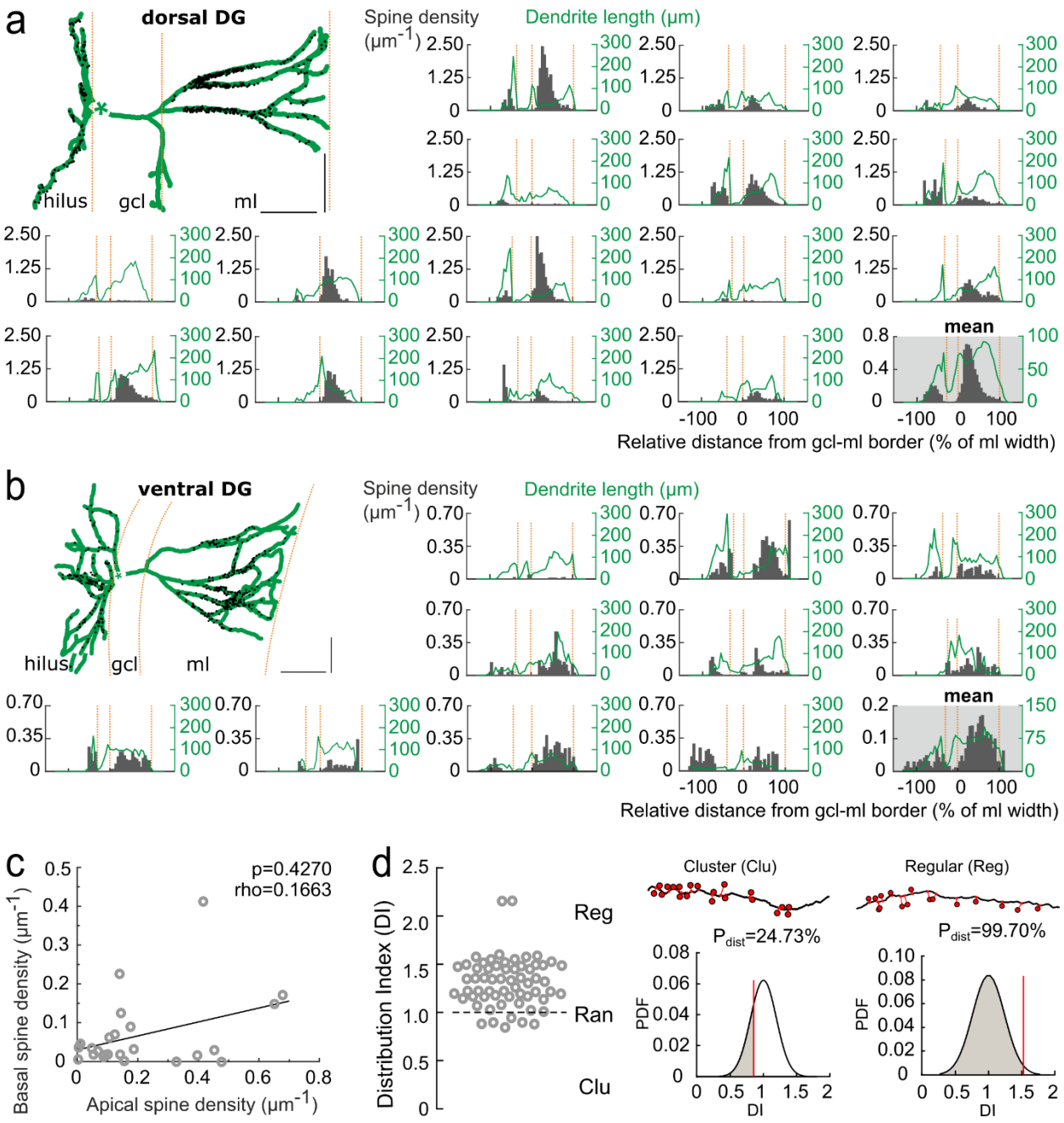

Supplementary Figure 2: Spine distribution on apical and basal PVI dendrites in the dorsal and ventral DG. a *Top left*, a representative 2D projection of the reconstructed dendritic arborization of a PVI (green) with dendritic spines depicted as black dots and the soma location represented with an asterisk. Red lines indicate the hilus-to-granule cell layer (gcl) border, the gcl-to-molecular layer (ml) border and the alveus. Histograms represent spine densities (dark gray) along the radial axis of PVI dendrites and the corresponding dendritic length (green line) of an individual PVI. Summary chart with group averages is

shown on the bottom right (mean). **b** Similar to **a,** but for PVIs from the ventral DG. Note the lacking asymmetric spine distribution at apical dendrites of the vDG, which we observed in the dDG. **c** Spine density on apical dendrites plotted against the density on basal dendrites for 25 PVIs shown in **a** and **b** indicting a lacking relationship in spine densities between basal and apical dendrites. **d** *Left*, spine distribution index (DI) of individual PVI segments (62 segments, 29 cells) in the inner and middle ml determined by Monte Carlo Simulation (see **Methods**). Note most data points are located at DIs>1 indicating regular spine arrangement. DI=1 random distribution and DI<1 clustered arrangement of PVI spines. *Right*, example of a rarely observed dendritic segment with clustered and a predominantly observed dendritic segment with regularly distributed spines. The probability density function (PDF) of 5.000 randomly bootstrapped spine positions is plotted against DI (see **Methods** for details). P_{dist} refers to the probability that the spine distribution is clustered ($P_{dist} < 0.05$) or regular ($P_{dist} > 0.95$) when compared to a randomly distributed spine population. Circles in (c) represent individual cells and in (d) individual dendritic segments related to individual PVIs. Scale bars: (a) and (b) 50 µm.

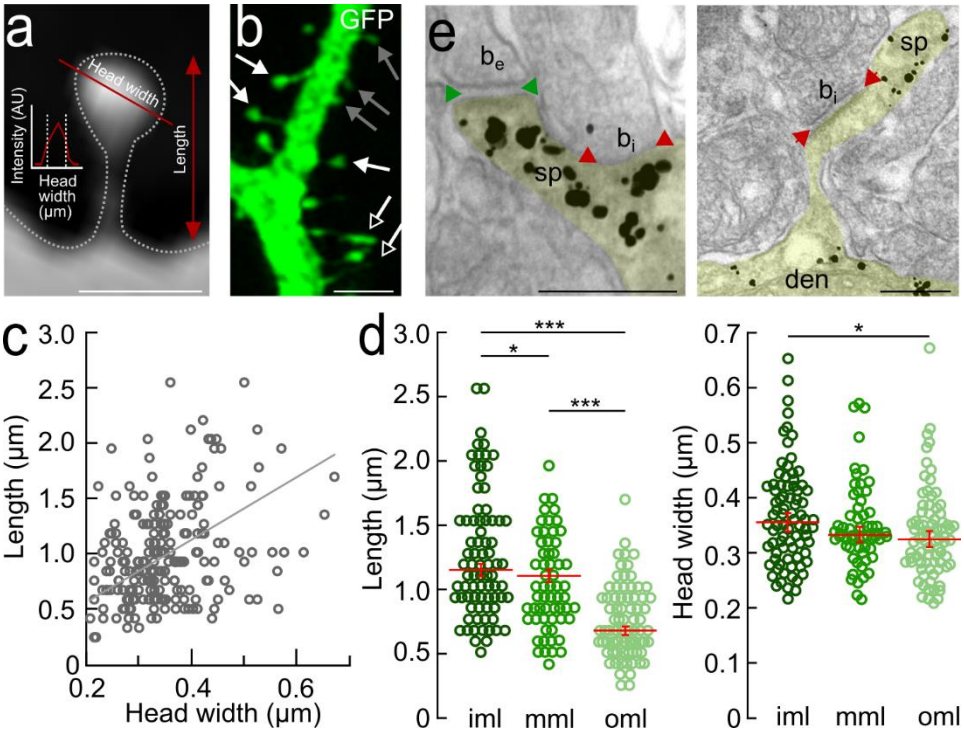

Supplementary Figure 3: Properties of spines on apical dendrites of dorsal DG PVIs. a Illustration of how head width and length of individual spines was determined. The intensity of the fluorescence signal across the head was plotted against its width from individual spines and the signal distribution was fitted with a Gaussian function to determine the head width. Length is the distance between the attachment point to the parent dendritic shaft and the spine tip (see **Methods**). **b** Dendritic segment of an AAV-FLEX-GFP expressing PVI shows the high morphological variability of spines ranging from small stubby (grey arrows), thin (black filled arrows), to spines with a thin neck and bulbous head (white arrows). **c** Spine length plotted against the corresponding head width (217 spines, 5 mice; rho = 0.30; $P = 6.8 \times 10^{-6}$, Spearman's correlation coefficient). **d** *Left*, spine length and *right,* head width of PVI spines along the radial axis of the dDG (inner ml, iml; middle ml, mml; outer ml, oml; 80 spines in inner ml, 60 in middle ml and 77 in outer ml, 217 spines; 5 mice; length: $P=2.78 \times 10^{-12}$, Kruskal-Wallis test; iml vs mml, $P=0.01$, iml vs oml, $P=2.17 \times 10^{-12}$, mml vs oml $P=3.55 \times 10^{-6}$, Wilcoxon-Mann-Whitney-test; head width: $P=0.03$, Kruskal-Wallis test; iml vs oml $P=0.01$, iml vs mml $P=0.23$, mml vs oml $P=0.19$, Wilcoxon-Mann-Whitney-test for spine comparisons). **e** Spines (*sp*) of PVIs (gold particles, yellow overlay) established asymmetrical (green) and symmetrical (red) boutons (*b*) with putative excitatory (green, b_e) and inhibitory (red) boutons (b_i), respectively, as detected by the pre-

53 embedding immunogold method (*den*, dendrite). Circles represent individual spines. *P<0.05; ***P<0.001.

54 Scale bar in (a) 1 µm, in (b) 2 µm, in (e) 250 nm.

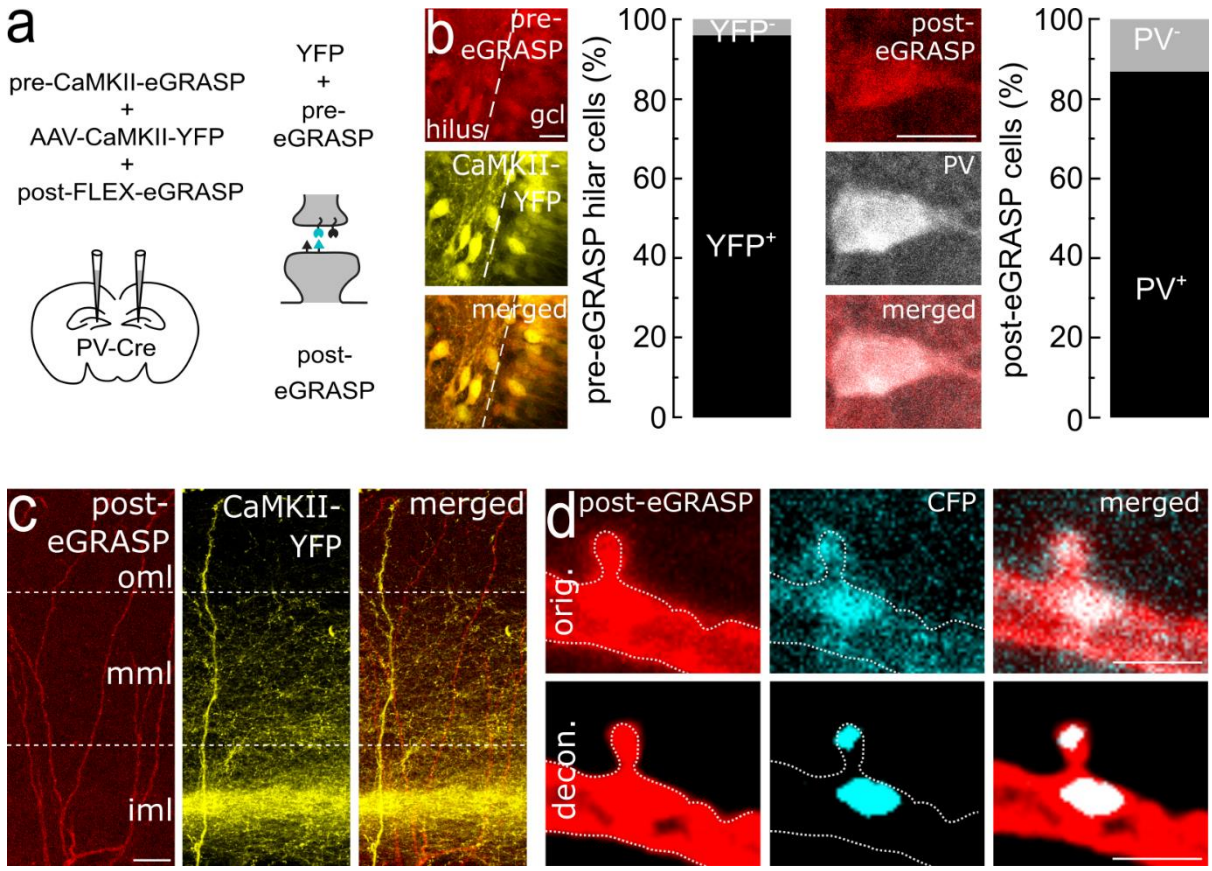

Supplementary Figure 4: PVI spines are contacted by glutamatergic synapses. a Same as in **Fig. 2b**, l*eft*, schematic illustration of AAV-pre-CaMKII-eGRASP, AAV-post-FLEX-eGRASP-RFP and AAV-CaMKII-YFP injections into the dDG of PV-Cre mice. *Right*, schematic illustration of dual-eGRASP fragments reconstituting to a functional CFP^+ signal. **b** *Left*, confocal image stacks show (*top*) principal cell somata in the gcl (GCs) and hilus (mossy cells; MCs) co-expressing pre-eGRASP (red) and AAV-CaMKII-YFP (yellow, *middle*) to trace axons, and the merged images (*bottom, orange*). Bar graph shows high co-localization of pre-eGRASP in hilar MCs with CaMKII-YFP (96%, 173 cells, 2 mice). *Right*, confocal image stacks show a post-eGRASP expressing PVIs (*top*, red) and its immunopositivity for PV (*middle*, white). Bar graph summarizes the high fraction of post-eGRASP expressing PVIs co-localizing PV (87%, 38 PVIs, 2 mice). **c** Confocal image stacks of ml containing axons of contralaterally projecting YFP^+-MC axons (yellow) and apical dendritic tree of a post-$eGRASP^+$ PVIs (red). **d** *Left,* confocal images of a dendritic segment of a post-eGRASP-expressing PVI (red) with reconstituted CFP^+ before (*top row*) and after (*bottom row*) deconvolution. Scale bars in (b, c) 20 µm, (d) 2 µm.

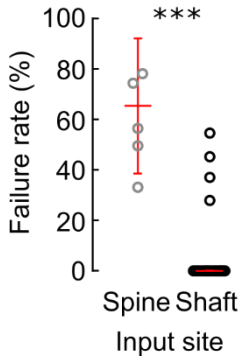

Supplementary Figure 5: PVI spine inputs show higher failure rate. Failure rate of calcium signals evoked by extracellular stimulation in close vicinity of a visually identified spine during 2-Photon imaging of PVIs filled with a whole-cell recording pipette with OGB1- and AlexaFluor 594 *in vitro* (spine vs shaft: 63.8% vs 8.4% failure rate, 6 spines, 20 shafts from 6 and 5 PVIs, respectively; P=1.16x10^{-4}, unpaired two-sided t-test). Circles represent individual data points obtained from spines or shafts.

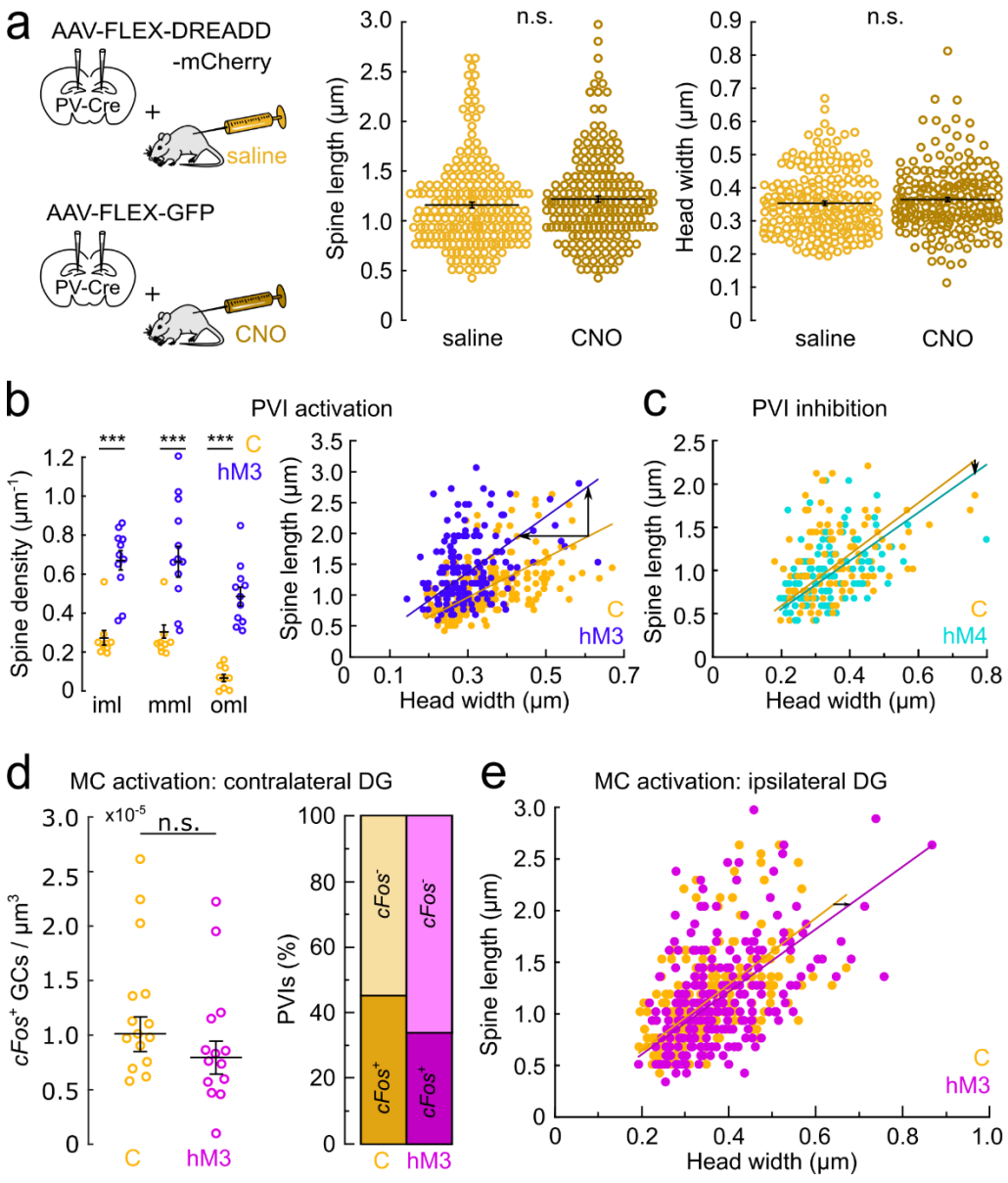

Supplementary Figure 6: Chemogenetic stimulation of PVIs elevates their spine density whereas input activation results spine head enlargement. a *Left*, illustration of control experiments. *Upper*, PV-Cre mice, injected with AAV-FLEX-hM3Dq-mCherry in the dDG, received three intraperitoneal saline injections every 8hs. *Lower*, PV-Cre mice injected with AAV-FLEX-GFP received CNO injections (**Methods**). *Right*, summary plots show lacking unspecific effects of CNO on spine properties (saline: 211 spines, 11 PVIs, 4 mice; CNO: 214 spines, 9 PVIs, 2 mice; length: P=0.07, head width: P=0.12, Wilcoxon-Mann-Whitney-test, spine comparisons). **b** *Left*, spine densities of hM3Dq-PVIs in the dDG of mice injected with saline (C, yellow, 9 cells, 4 mice) and mice injected with CNO (hM3Dq, blue; 11 cells, 3 mice). Spine

densities for dendritic segments in the inner, middle and outer ml (C vs hM3Dq: iml P=0.0004, mml P=0.001, oml P=0.0002, unpaired two-sided t-test for cell comparisons). *Right*, length plotted against head width for individual PVI spines from control and hM3Dq-expressing mice. Note shift of the linear fit to the data indicating enhanced length and reduced head width in hM3Dq-PVIs (C vs hM3: rho=0.54 and 0.29, P=2.19x10^{-17} and P=0.0002, respectively, Spearman's correlation for spines; same data as in **Fig. 4g**). **c** Similar to b for control and hM4Di-PVIs. Note a mild shift towards lower spine length in hM4Di-PVIs (C vs hM4: rho=0.32 and 0.46, respectively; P=0.0002 and P=1.02x10^{-7}, Spearman's correlation for spines; same data as in **Fig. 4g**). **d** Stimulation of hM3Dq-PCs in the ipsilateral dDG (GCs, MCs) had no effect on the number of *cFos*$^{+}$ GCs normalized to the gcl volume per slice and on PVIs normalized to the total PVI population per slice in the contralateral dDG (C, yellow; GCs, C vs hM3Dq: 15 vs 10 slices, 454 and 660 cells, respectively; 5 mice per group; P=0.08 Wilcoxon-Mann-Whitney-test, slice comparisons; PVIs, C vs hM3Dq: 86 vs 65 cells, 12 and 11 slices, respectively; 5 mice per group; P=0.15 Fisher's exact test, slice comparisons). **e** Spine length plotted against head-width for individual PVI spines of the contralateral dDG in saline controls (C, yellow) and in hM3Dq-PVIs stimulated by CNO (pink; C vs hM3Dq: 211 vs 238 spines, 4 and 3 mice, respectively; rho=0.54 and 0.49; P=2.19x10-^{17} and P=6.95x10^{-16} Spearman's correlation coefficients). ***P<0.001, n.s. P≥0.05; black lines represent means ± SEM. Circles in (a, b right, c and e) indicate individual spines and in (b left, d) cells.

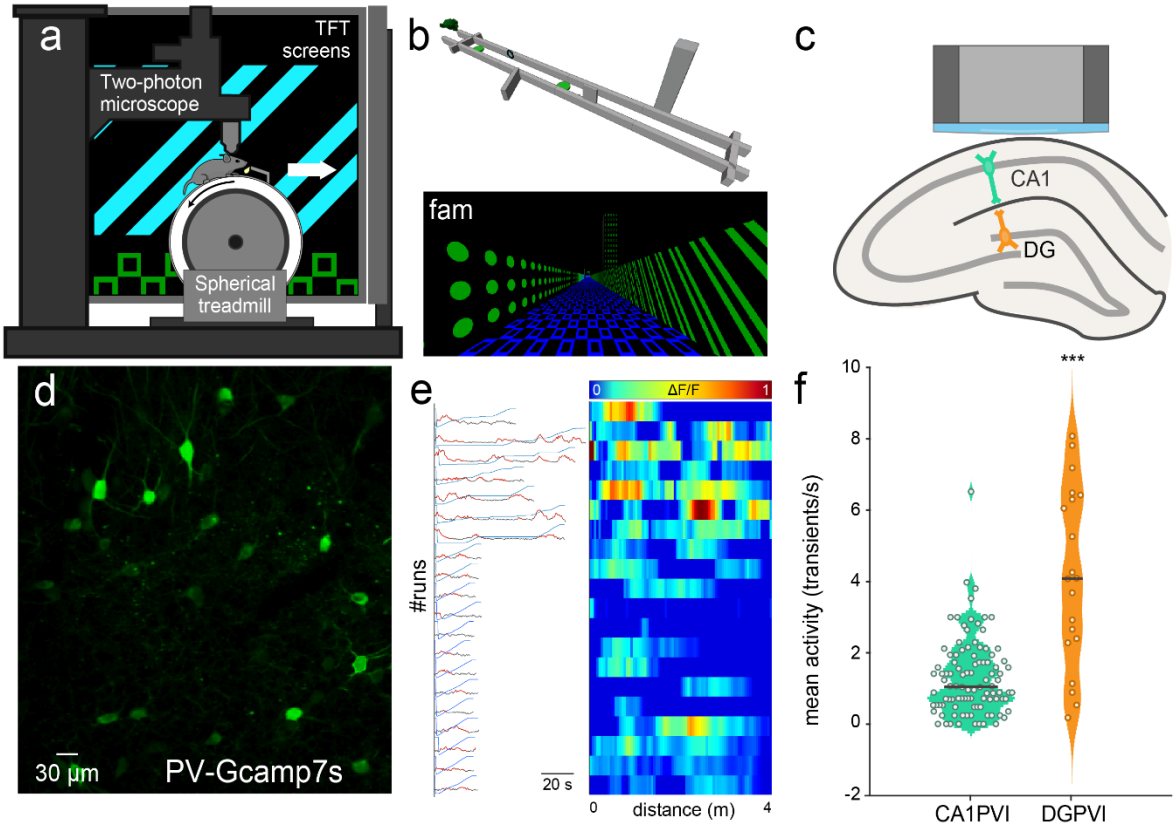

Supplementary Figure 7: Recording of CA1 and DG PVI activity in head-fixed mice navigating through virtual environment. a Schematic of the recording setup. **b** *Upper,* virtual linear track. Green circles indicate reward sites. Gray bars indicate their location on the linear track in the virtual reality. *Lower*, behavioral layout. **c** Schematic of the window implantation (**Supp. Methods**). **d** Image illustrates time-averaged GCaMP7s (green) fluorescence signal of CA1 PV-cells obtained *in vivo*. **e** *Left* Fluorescence signal (black line), transients detected (red) and position on the linear track (blue line) of a representative DG PVI over time. *Right,* activity (color-coded) of the same PVI as a function of position on the familiar linear track over multiple trials. **f** Distribution of mean activity rate (transient rate min^{-1}) during running in the familiar environment. *** $P = 2.42 \times 10^{-13}$, two-sides Student's t-test ANOVA (CA1 100 PVIs, 3 mice; DG 24 PVIs, 4 mice). Black and gray lines indicate mean ± SEM; circles represent individual PVIs. Mean running speed is not significantly different between DG and CA1 (two-sides Student's t-test ANOVA P=0.8294; mean running speed 16.7cm/s).

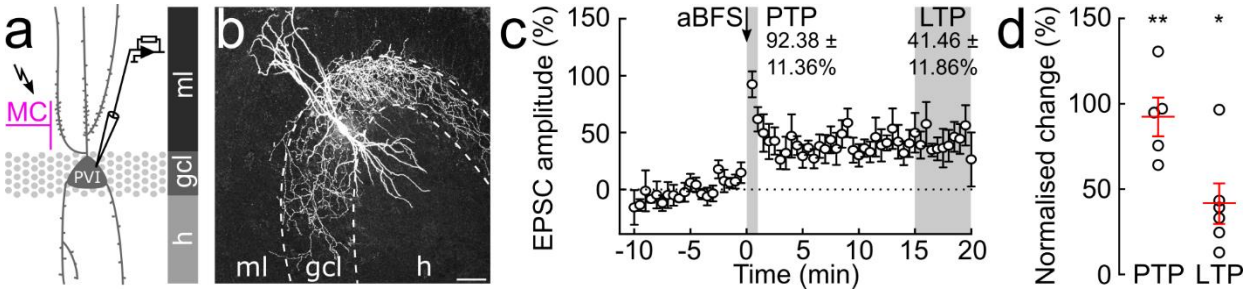

Supplementary Figure 8: Electrical stimulation of mossy cell-PVI inputs leads to Hebbian long-term potentiation. a Schematic illustration of the experimental design. Whole-cell recordings of PVIs in acute slices during extracellular mossy cell (MC, magenta) axon stimulation in the inner molecular layer (ml). **b** Confocal image of a basket cell loaded during recordings with biocytin and visualized with AlexaFluor 647 conjugated with avidin. Note axonal distribution concentrated to the granule cell layer (gcl). **c** Peak amplitudes of EPSC normalized to the mean preceding baseline before, during and after application of an associative 30 Hz burst frequency stimulation (aBFS); arrow indicates time of aBFS application (12 bursts of stimuli delivered at 0.3 Hz; each burst composed of 25 stimuli applied at 30 Hz; Sambandan et al. 2010). A post-tetanic potentiation (PTP; 92.4 ± 11.4% of baseline) is followed by a long-term potentiation (LTP). Gray bars represent the time window for PTP and LTP quantification (see **Methods**). **d** Plot summarizes PTP (5 cells; P=0.001, two-sided t-test) and LTP (41.5 ± 11.9% of baseline, 15-20 min after aBFS; 6 cells; P=0.02, two-sided t-test) at MC-PVI synapses. *P<0.05; **P<0.01. Circles in (c) are averages of EPSCs over 30 sec of the cell shown in (b), in (d) represent individual cells. Black and red lines indicate mean ± SEM; h, hilus.

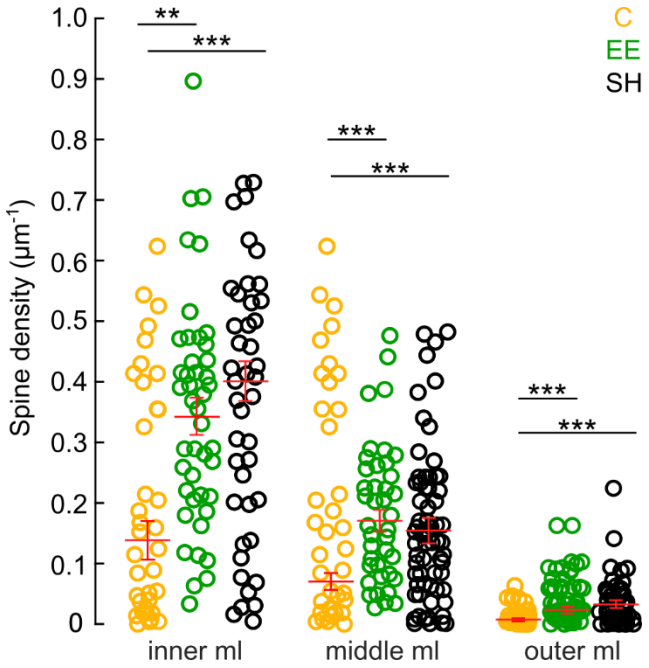

131

132 **Supplementary Figure 9: Experience-dependent increase in spine density in dDG PVIs emerges in**
133 **the inner, middle and outer molecular layer.** Spine density of dDG PVIs in the inner, middle or outer
134 molecular layer (ml) of mice kept under control (C), enriched environment (EE) or single housing (SH)
135 conditions (C vs EE vs SH: 36 vs 40 vs 43 cells from 5, 7 and 7 mice, respectively; inner ml: P=0.0007,
136 Kruskal-Wallis test; C vs EE P=0.001, C vs SH P=0.0009, Wilcoxon-Mann-Whitney-test; middle ml:
137 P=0.0001, Kruskal-Wallis test, C vs EE P=4.44x10^{-5}, C vs SH P=0.0007, Wilcoxon-Mann-Whitney-test;
138 outer ml: P=0.0002, Kruskal-Wallis test, C vs EE P=0.0003, C vs SH P=0.0005, Wilcoxon-Mann-Whitney-
139 test). Circles represent individual cells. Red lines indicate median ± SEM.

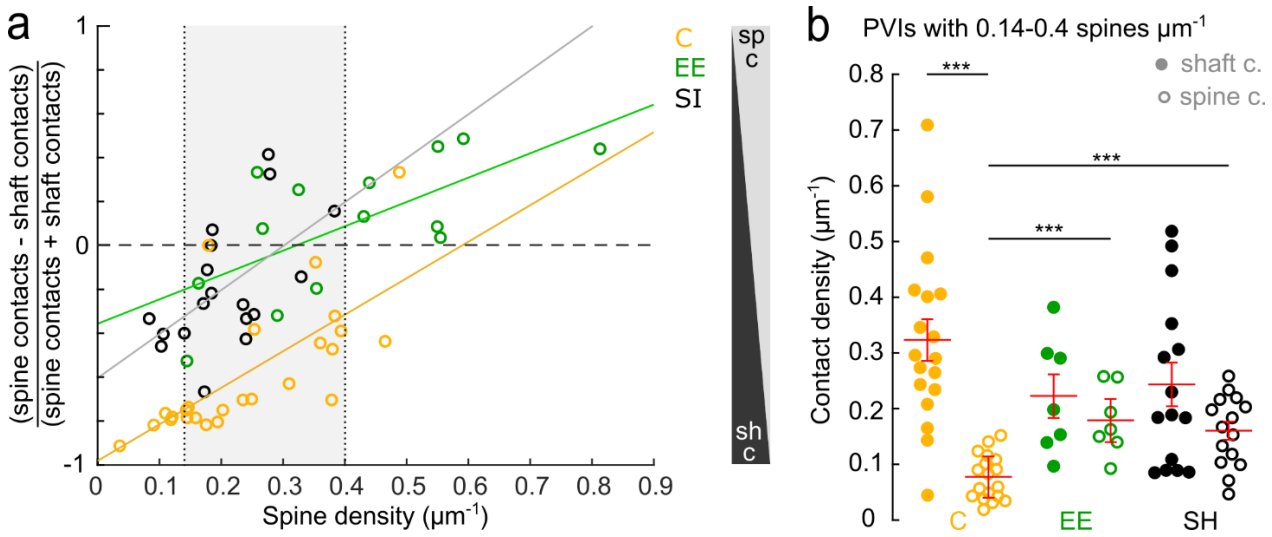

Supplementary Figure 10: MC-PVI synapses redistribute from PVI shafts to spines after experiencing EE or SH. a Normalized fraction of dual-eGRASP labeled MC-PVI synapses at PVI dendritic shafts and spines located in the inner molecular layer plotted against spine density for control (yellow), EE (green) and SH (black) conditions. Linear fits to the data indicate that the fraction of MC-PVI contacts located at spines (sp-c) linearly increases with spine density (-1<x<0 inputs at shafts dominate; 0<x<1 inputs at spines dominate) to the costs of shaft contacts (sh-c). Same set of data as shown in **Fig. 8c** (C vs EE vs SH: 25 vs 14 vs 18 PVIs including 83, 66 and 76 analyzed dendritic segments from 4, 3 and 3 mice, respectively; 1410, 1034 and 952 MC-PVI contacts and 803, 728 and 584 spines were analyzed in relation to C, EE and SH; C rho=0.80, P=1.36x10^{-4}; EE rho=0.57, P=0.016; SH rho=0.67, P=0.008; Spearman's correlation for individual PVIs). **b** Similar data as **Fig. 8c;** input density at PVI spines (open circles) and shafts (filled circles) under conditions of control, EE and SH are shown for cells with 0.14-0.4 spines µm^{-1} dendritic length. Since the fraction of MC-PVI inputs at spines depends on spine density (see a), we selected here a fraction of PVIs with a spine density range found in all three behavioral conditions (shaded area in a). Note that similar to **Fig. 8c**, input density at dendritic shafts declines but increases at spines under conditions of EE and SH (C vs EE vs SH: 17 vs 7 vs 15 PVIs with 61, 31 and 66 analyzed dendritic segments from 4, 3 and 3 mice, 949, 392 and 831 MC-PVI contacts and 601, 245 and 532 spines, respectively; P=3.94x10^{-7}, one-way ANOVA; shaft contacts vs spine contacts: C P=2.90x10^{-7}; EE P=0.35; SH P=0.06; shaft vs shaft contacts: C vs EE, P=0.14; C vs SH, P=0.15; EE vs SH, P=0.74; spine vs spine

contacts: C vs EE, P=5.86x10^{-5}; C vs SH, P=7.12x10^{-5}; EE vs SH, P=0.52; unpaired two-sided t-test for cell comparisons). *P<0.05, **P<0.01, ***P<0.001. Circles represent data of individual cells.

Supplementary Methods (Supplemental Fig. 7)

Mice. All experiments involving animals were carried out according to national and institutional guidelines and approved by the 'Tierversuchskommission' of the Regierungspräsidium Freiburg (license no. G16/037) in accordance with national legislation. We used a total of 5 PV-Cre (B6;129P2-Pvalbtm1(Cre)Arbr/J; Jackson laboratory).

Virus injections and head plate implantation: All surgical procedures were performed in a stereotactic apparatus (Kopf instruments) under anesthesia with 1-2% Isoflurane and analgesia using 0.1 mg kg^{-1} buprenorphine. A small (~0.5 - 1 mm diameter) craniotomy was made over the hippocampus and 400 nl of AAV9-syn-FLEX-GCaMP7s-WPRE (titer $3*10^{12}$ viral genomes ml^{-1}; University of Pennsylvania Vector Core) was injected into CA1 or DG (a/p: -1.5 mm; m/l -1.5 mm; v -1.4 or -1.8 mm) in PV-Cre mice. Together with the viral injection, mice were implanted with a stainless-steel head plate oriented horizontal (25 x 10 x 0.8 mm with an 8 mm central aperture) in the same surgery session. Mice were allowed to recover from surgery for at least 5 days before training sessions commenced. Postoperative analgesic treatment was continued with carprofen (5 mg kg^{-1} body weight) for 3 days after surgery.

Imaging window implantation: Cortical excavation and imaging window implantation were performed >10 days after the initial virus injection, according to published protocols[22]. A craniotomy (diameter 3 mm) was made centered at a/p -1.5 mm and m/l -1.5 mm for DG and CA1 imaging. Parts of the somatosensory cortex as well as posterior parietal association cortex were gently aspirated while irrigating with chilled saline. We continued aspiration until the external capsule was exposed. The outer part of the external capsule was then gently peeled away using fine forceps leaving the inner capsule and the hippocampus itself undamaged. The imaging window implant consisted of a 3 mm diameter coverslip (CS-3R, Warner Instruments) glued to the bottom of a stainless-steel cannula (3 mm diameter 1.2-1.5 mm height). The window was gradually lowered into the craniotomy using a forceps until the glass was in contact with the external capsule. The implant was then affixed to the skull using cyanoacrylate. Mice were allowed to recover from window implantation for 2-3 days.

Virtual environment setup and behavioral training. Our custom virtual environment setup, described in detail in[22], consisted of an air-supported polystyrene ball (20 cm diameter). Motion of the ball was monitored

with an optical sensor (G-500, Logitech) and translated into forward motion through the virtual environment. The forward gain was adjusted, so that 4 m of distance travelled along the circumference of the ball equaled one full traversal along the linear track. The virtual environment was displayed on four TFT monitors (19" screen diagonal, Dell) arranged in a hexagonal arc around the mouse and placed ~25 cm away from the head, thereby covering ~260° of the horizontal and ~60° of the vertical visual field of the mouse. The virtual environment was created and simulated using the open-source 3D rendering software Blender. The track consisted of textured walls, floors and other 3D rendered objects at the track's sides as visual cues. The animal ran first for 60 s on one track and was then 'teleported' from its current position to the start of the other track and able to run for another 60 s after a brief (<10 s) pause, in which the screens were blanked. To motivate consistent behavior, soy-milk rewards (2 µl) were administered when the animal traversed certain locations that were spread at fixed distances along the track.

Five days after head plate implantation, mice were placed in the virtual environment for 10-30 min daily, with gradually increasing timespans. After 4-5 days of habituation, mice showed consistent running. Mice were thereafter implanted with the cortical window and allowed to recover from the surgery. After recovery, training in the virtual environment was re-initiated for 30-60 min daily in the familiar context until consistent running was observed in all animals and familiarization to the context had been achieved for at least 10 days in total before start of the imaging sessions. Data were obtained from the runs in the familiar environment during one day.

In vivo two-photon calcium imaging. Imaging was performed using a resonant/galvo high-speed laser scanning two-photon microscope (Neurolabware) with a frame rate of 30 Hz for bidirectional scanning and a power of 5-20 mW measured at the objective front-lens for both hippocampal subfields. The microscope was equipped with an electrically tunable, fast z-focusing lens (optotune, Edmund optics) to switch between z-planes within less than a millisecond. Images were acquired through a 16x objective (Nikon, 0.8 N.A., 3 mm WD). GCaMP7s was excited at 930 nm with a femtosecond-pulsed two-photon laser (Mai Tai DeepSee®, Spectra-Physics). We scanned three imaging planes (~25 µm z-spacing between planes) in rapid alternation so that each plane was sampled at 10 Hz. The planes spanned 300-500 µm in x/y-direction and were placed so that as many labelled neurons as possible were depicted. To block ambient light from

the photodetectors, the animals head plate was attached to the bottom of an opaque imaging chamber before each experiment and the chamber was fixed in the behavioral apparatus together with the animal. A ring of black foam rubber between the imaging chamber and the microscope objective blocked any remaining stray light.

Histology and detection of imaging area. At the end of experiments, mice were deeply anaesthetized using ketamine/xylazine (Sigma Aldrich) and image stacks of the area underneath the imaging window were acquired *in vivo* in the two-photon microscope. Mice were then perfused transcardially with 4% paraformaldehyde in phosphate-buffered saline (PBS). Brains were cut in 100 µm coronal slices and sections containing the area underneath the imaging window were collected. Image stacks of GCaMP7s and mRuby2 fluorescence in the sections were acquired with a confocal microscope (LSM 710, Zeiss) and the imaged region was re-identified by comparing these stacks with the ones obtained *in vivo,* as described[22].

Imaging data processing, segmentation and data extraction. Motion correction of all imaging data was performed line-by-line using the SIMA software package with a 2D Hidden Markov Model or with the software-package 'Suite2P' as previously applied[22]. If no decent motion correction could be achieved, the data were discarded. The motion-corrected and time-averaged image of mRuby2 for each run was used to align recordings from the same field of view relative to each other and their displacements were stored with the dataset.

To segment interneuron somata, regions of interest (ROIs) were drawn manually using ImageJ (NIH) or automatically by applying the 'suite2P' software package[71]. In case of automated ROI settings, individual ROIs were subsequently inspected by the experimenter. Cell bodies were identified based on the motion-corrected, time-averaged GCaMP7s and mRuby2 fluorescence images. The obtained ROIs were transformed according to the displacement between the mean mRuby2 fluorescence images as described above and the average calcium signal over time was obtained from each ROI for all runs. We restricted our analysis to running periods of mice with a minimum speed of 4 $cm*s^{-1}$.

For hippocampal principal cells, individual transients were detected as previously described[22,72]. In brief, calcium traces were corrected for slow changes in fluorescence by subtracting the 8th percentile value of

the fluorescence-value distribution in a window of ~8 s around each time point from the raw fluorescence trace. We obtained an initial estimate on baseline fluorescence and standard deviation (SD) by calculating the mean of all points of the fluorescence signal, which did not exceed 3 standard deviations (SD) of the total signal and would therefore be likely to be part of a significant transient. We divided the raw fluorescence trace by this value in order to get obtain a $\Delta F/F$ trace. We used this trace to determine the parameters for transient detection that yielded a false positive rate (defined as the ratio of negative to positive going transients) <5% and extracted all significant transients from the raw $\Delta F/F$ trace. Definitive values for baseline fluorescence and baseline SD were then calculated from all points of this trace which did not contain significant transients. For further analysis, all values of this $\Delta F/F$ trace that did not contain significant calcium transients were masked and set to zero. For hippocampal INs, rigorous identification of spike or burst-related calcium transients is often prevented by their high firing rates, which exceeds the acquisition rate of our imaging system and the kinetics of the calcium indicator[73]. However, the calcium signal from INs can still be used to approximate their firing rate over time[74]. To obtain baseline-normalized $\Delta F/F$ calcium traces, we examined the fluorescence value distribution from each recording segment (containing 60 s familiar-track and 60 s novel-track running and a brief blank interval) and divided the entire trace by the 8^{th} percentile value of this distribution[22].

Supplemental Literature – Methods only

68. Leutgeb JK, Leutgeb S, Moser MB, Moser EI. Pattern separation in the dentate gyrus and CA3 of the hippocampus. *Science* **315,** 961-966 (2007).

69. Booker, S. A. *et al.* KCTD12 Auxiliary Proteins Modulate Kinetics of GABA $_B$ Receptor-Mediated Inhibition in Cholecystokinin-Containing Interneurons. *Cereb. Cortex* **27**, 2318–2334 (2016).

70. Buhl, E. H. *et al.* Physiological properties of anatomically identified axo-axonic cells in the rat hippocampus. *Journal of Neurophysiology* **71**, 1289–1307 (1994)

71. Pachitariu, M. *et al. Suite2p: beyond 10,000 neurons with standard two-photon microscopy*. http://biorxiv.org/lookup/doi/10.1101/061507 (2016) doi:10.1101/061507.

72. Dombeck, D. A., Harvey, C. D., Tian, L., Looger, L. L., Tank, D. W. Functional imaging of hippocampal place cells at cellular resolution during virtual navigation. *Nat Neurosci* **13**, 1433–1440 (2010).

73. Chen, T.-W. *et al.* Ultrasensitive fluorescent proteins for imaging neuronal activity. *Nature* **499**, 295–300 (2013).

74. Geiller, T. *et al.* Large-Scale 3D Two-Photon Imaging of Molecularly Identified CA1 Interneuron Dynamics in Behaving Mice. *Neuron* S0896627320307133 (2020) doi:10.1016/j.neuron.2020.09.013.